

Comprehensive evaluations of a Prototype Full Field-of-View Photon Counting CT System through Phantom Studies

Xiaohui Zhan^{1,*}, Ruoqiao Zhang¹, Xiaofeng Niu¹, Ilmar Hein¹, Brent Budden¹, Shuoxing Wu¹, Nicolay Markov¹, Cameron Clarke¹, Yi Qiang¹, Hiroki Taguchi², Keiichi Nomura³, Yoshihisa Muramatsu³, Zhou Yu¹, Tatsushi Kobayashi³, Richard Thompson¹, Hiroaki Miyazaki², Hiroaki Nakai²

¹Canon Medical Research USA, Inc., 706 Deerpath Drive, Vernon Hills, IL, USA 60061

²Canon Medical System Corporation, Otawara, Tochigi, Japan

³National Cancer Centre Hospital East, 6-5-1 Kashiwanoha, Kashiwa, Japan

ABSTRACT

Photon counting CT (PCCT) has been a research focus in the last two decades. Recent studies and advancements have demonstrated that systems using semiconductor-based photon counting detectors (PCDs) have the potential to provide better contrast, noise and spatial resolution performance compared to conventional scintillator-based systems. With multi-energy threshold detection, PCD can simultaneously provide the photon energy measurement and enable material decomposition for spectral imaging. In this work, we report a performance evaluation of our first CdZnTe-based prototype full-size photon counting CT system through various phantom imaging studies. This prototype system supports a 500 mm scan field-of-view (FOV) and 10 mm cone coverage at isocenter. Phantom scans were acquired using 120 kVp from 50 to 400 mAs to assess the imaging performance on: CT number accuracy, uniformity, noise, spatial resolution, material differentiation and quantification. Both qualitative and quantitative evaluations show that PCCT has superior image quality with lower noise and improved spatial resolution compared to conventional energy integrating detector (EID)-CT. Using projection domain material decomposition approach with multiple energy bin measurements, PCCT virtual monoenergetic images (VMIs) have lower noise, and superior performance in quantifying iodine and calcium concentrations. These improvements lead to increased contrast-to-noise ratio (CNR) for both high and low contrast study objects and can significantly reduce the iodine contrast agent to achieve the same CNR as EID-CT. PCCT can also generate super-high resolution (SHR) images using much smaller detector pixel size than EID-CT and dramatically push the spatial resolution limit. These initial results demonstrate that PCCT based on CdZnTe detectors has huge potential in clinical settings.

* Send correspondence to Xiaohui Zhan <xzhan@mru.medical.canon>

Keywords: X-ray Computed Tomography, photon counting detector, spectral imaging, high resolution, image quality

1. INTRODUCTION

New CT systems using semiconductor detector are under active research and development [1][2][3][4]. As an emerging technology, it has been introduced for experimentation and prototyping since decades ago. Recently, the first PCCT clinical product was released and marks a new era for wider clinical adoption [5]. Many studies have demonstrated its superior performance and the associated benefits in various clinical applications to conventional energy-integrating detector (EID) CT [4][6][7][8][9][10]. For conventional scintillator-based EID [11], the measurement needs a two-step conversion process: the absorbed photon energy is first converted to optical photons, and then optical photons are converted to electrical signals through a photodiode. As a result, the amplitude of the signal is proportional to the photon energy, and the lower energy photons that have more material resolving power are downweighed. Another limitation from such an energy integrating process is that the electronic noise from the front-end electronics will always be part of the measurement. When the number of photons is low, the electronic noise becomes dominant and gradually degrades the image quality. In addition, between the scintillator pixels, a reflector of finite thickness is needed to prevent optical crosstalk, which increases the dose penalty when the pixel size gets small. All these limitations in EID can be largely mitigated or resolved in photon counting detector (PCD), for which the absorbed photon energy is converted to an electric signal directly. Instead of measuring the total energy deposited in each time interval for EID, PCD measures the energy of each incident photon. This type of measurement results in an equal weighting of the transmitted photons and effectively removes the front-end electronic noise by setting a proper triggering threshold. The whole detector is active without the need for reflective material between pixels and allows for smaller pixel size without dose penalty. With multiple energy bin measurement, spectral information can be simultaneously obtained for spectral imaging which is achieved by the current dual energy (DE) EID-CT [12][13], either by using a dual-source spectrum, fast kVp switching or dual-layer EID technology. Moreover, with a flexible energy threshold setting, PCD allows measurements to target specific K-edge high Z materials and enables K-edge imaging from common contrast agents such as iodine and gadolinium to novel nanoparticles [15][14][16][17].

For the detector materials, CdTe and CdZnTe are the most common room temperature semiconductors for such applications, benefiting from their wide band gap, high density, and high effective atomic number. CdTe has a longer history but typically suffers from a higher dark current and is more prone to polarization, as compared

to CdZnTe. Both materials face challenges with regards to manufacture (brittleness) and performance (e.g., thermal stability, charge trapping). Furthermore, due to the nature of the detection physics processes in these semiconductor materials, the detector spectral response usually degrades from ideal because of effects such as x-ray fluorescence (k-escape), Compton scattering, charge sharing, as well as pulse pileup and other complications from the associated front-end electronics [18][19]. In order to assess the practical benefits of PCCT compared to conventional EID-CT with all these non-ideal factors and explore potential new applications, a CdZnTe-based full-size photon counting CT prototype system has been built and studied.

In this manuscript, we first introduce the key technical aspects of our engineering prototype photon counting CT system, followed by a series of phantom studies for a comprehensive assessment of its image quality. Example images from this prototype system associated with qualitative and quantitative analysis results are presented and discussed. In particular, some of the key studies are directly compared with a Canon conventional EID-CT to demonstrate the differences introduced by PCD. In the end, we give a brief summary and outlook to the future system development plan.

2. MATERIALS AND METHODS

System Description

The engineering prototype PCCT system is built based on a Canon Aquilion ONE ViSION CT gantry. The CdZnTe-based photon counting detector array populates the full 500 mm FOV in the fan angle and covers up to 9.92 mm in the cone direction at isocenter. A 1-D ASG is placed on top of the detector plane to reduce scattered photons. As illustrated in Figure 1, for normal resolution (NR) mode, the readouts of a 3×3 grid of micro pixels are summed as input for image reconstruction, which produces the same in-plane detection pitch as that of Canon's conventional EID-CT. For super high resolution (SHR) mode, the readout of each micro pixel is used for processing and image reconstruction. Each detector pixel can output up to 6 energy bins of measurements starting from 20 keV. The counting mode generates images based on the events with photon energy greater than 30 keV, and the spectral mode generates images using 5 energy bins with threshold settings of 30/45/55/65/80 keV.

After the electrical charges are induced in the CdZnTe sensor from the incident photon, the signal goes through a series of processing in the front-end readout electronics (ASIC) and generates the counting measurements. The ASIC employs a charge-sensitive amplifier (CSA) and related circuitry design to allow fast triggering. Such readout is capable of a uniformly-distributed maximum event rate defined by the inverse of the elapsed

time (deadtime), and therefore follows a non-paralyzable detection model [19]. Optimal deadtime enhances maximum count rate while also allowing for sufficient collection of the induced charge. A typical counting curve for a pre-defined deadtime is shown in Figure 2, where observed count rates (OCR) are plotted against assumed incident count rates (ICR). The ASIC additionally performs a form of pileup correction to restore the baseline in the high flux regime where pulses overlap, mitigating spectral distortion. The integrated voltage signal for each pixel is filtered and fed to six energy discriminators where it is compared to pre-programmed reference levels and appropriate counters incremented.

The technical specifications of this engineering prototype together with the EID system used for comparison are given in Table 1. In this study, scans were all acquired in circular mode at 120 kVp with 1 second per rotation speed and tube current from 50 to 400 mA.

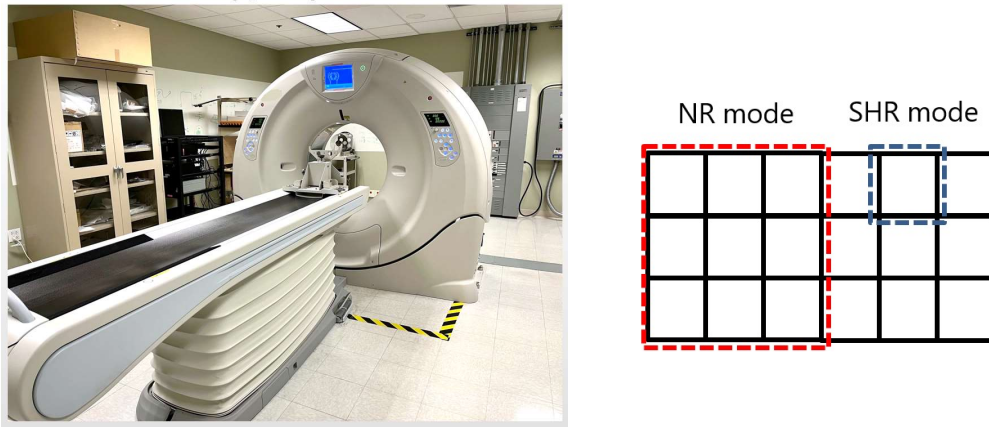


Figure 1: (Left) Canon's first engineering prototype PCCT system. (Right) An illustration of the prototype PCCT detector pixel readout schematic: the normal resolution (NR) mode combines the readout of a 3×3 micro pixels, and the SHR mode utilizes the readout of individual micro pixels for processing and image reconstruction.

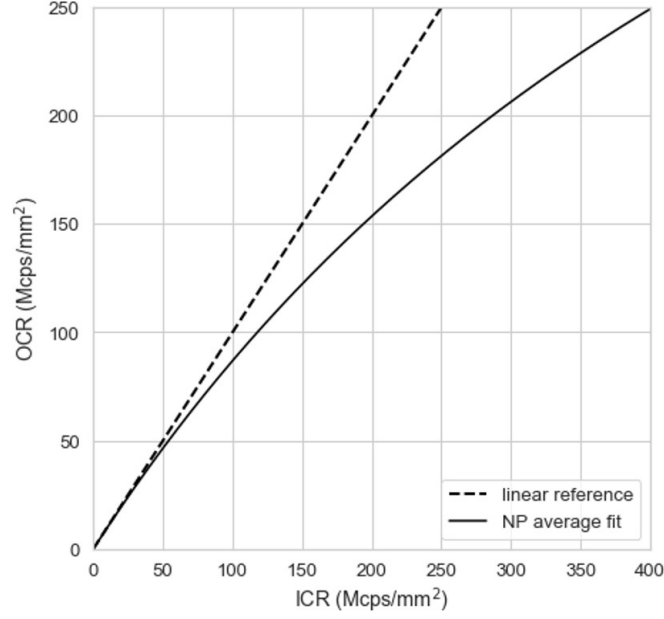


Figure 2: Typical PCD counting curve with a pre-programmed deadtime. It can be seen that the ASIC readout approximately follows a non-paralyzable detection model. When the incident count rate (ICR) increases, the observed count rate (OCR) gradually deviates from the ideal linear reference due to pulse pileup.

Table 1: Prototype system technical specification compared with a Canon EID-CT system

	Technical specification overview	
System	PCCT Engineering Prototype	EID-CT
Platform	Canon Aquilion ONE ViSION	
Detector material	CdZnTe	GOS + PDA
Collimation	16×0.62 mm (NR), 48×0.21 mm (SHR)	80×0.5 mm
Scan FOV	500 mm	
Tube voltage	120 kVp	
Tube current	50/100/200/400 mA	
Focal Size	Large (1.6 mm×1.5 mm), Small (0.9 mm×0.8 mm)	
Rotation speed	1 s	
Scan mode	Circular	
Readout mode	NR (3×3), SHR (1×1), 6 energy bins (20/30/45/55/65/80 keV)	NR
Recon	FBP	

The high-level data processing flow diagram is illustrated in Figure 3. For this prototype system, we configure it in a way that it always outputs data in micro pixel mode with all 6 energy bins to allow in-depth studies. After

scans, the measured projection data, energy bin counts N_i , first went through a few preprocessing steps including tube flux variation correction and data reformation. For the counting mode, counts with photon energy above 30 keV were summed for the counting line-integral sinogram estimation. During this step, the beam hardening correction was applied to account for the effect of the polychromatic beam spectrum. The counting line-integral sinogram then went through a filtered back-projection (FBP) reconstruction and some postprocessing steps to generate the counting image. For the spectral mode, 5 individual bin counts were used for a projection-domain material decomposition to generate 2 basis material (water/bone) pathlength sinograms [20][21]. Each of the basis material pathlength sinograms then went through an FBP reconstruction to generate the basis material images. The basis material images were then synthesized to generate the virtual monoenergetic images (VMIs) [22]. By using two different keV images, e.g., 60 keV vs. 90 keV, different materials can be properly classified and then quantified on such a 2-dimensional HU plot with the reference composition ground truth values.

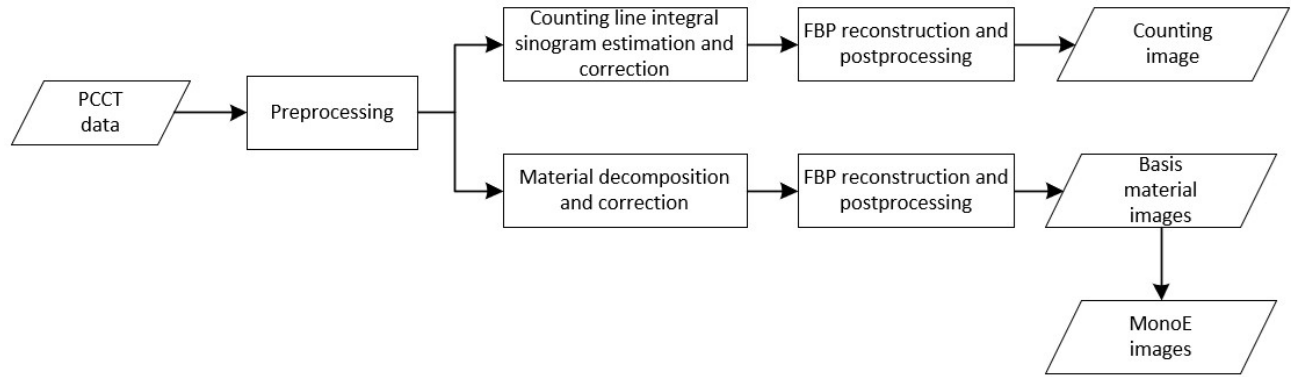


Figure 3: A high-level PCCT data processing flow diagram to generate counting and spectral images.

One of the major challenges in generating good image quality for PCCT is to accurately calibrate the detector response and establish a correct forward model [23][24][25][26]. In order to correct for the pixel-to-pixel detector response variation, each pixel needs a unique response calibration table as described in a generalized forward model below:

$$N_i(i = 1, \dots, n) = \int_{T_i}^{T_{i+1}} \Phi_i(E') \int_{E_{min}}^{E_{max}} N_0 S_0(E) D(E, E') e^{\int \mu L} dE dE'$$

$$\Phi_i = \begin{cases} 1, & T_i \leq E < T_{i+1} \\ 0, & \text{others} \end{cases}$$

Φ_i stands for the PCD ideal bin response function, and $S_0(E)$ and $D(E, E')$ represent the incident beam spectrum and detection response function, respectively. Their product was calibrated through a set of known attenuation samples. In order to achieve optimized image quality, a small number of mal-functioning pixels were excluded in the data processing.

Phantom Studies and Image Quality Evaluations

After a series of system and detector related calibrations, several phantoms were scanned at 4 different dose levels (50/100/200/400 mAs) and images were reconstructed for comprehensive evaluations on the following aspects:

- 1) CT number accuracy, uniformity
- 2) Spatial resolution and noise
- 3) Material quantification accuracy based on VMIs and contrast-to-noise ratio (CNR)

Through these evaluations, we explored the benefits of PCD measurements by acquiring the same phantom scans from a Canon EID-CT system (Aquilion ONE ViSION). For spectral image comparison, a sequential (rotate-rotate) dual energy scan mode (80/135 kVp) [13] was used on the EID-CT. With the same gantry geometry, X-ray tube, beam filtration, and image reconstruction kernels at matched radiation doses, one can perform a rigorous comparison between PCCT and EID-CT systems, and demonstrate the improvements introduced solely by the new detection technology and the associated changes.

CT number accuracy and uniformity were assessed using 1) a set of water cylindrical phantoms with diameters of 18/24/32/40 cm; and 2) a 32 cm diameter Canon TOS phantom with multiple material inserts (Figure 4). According to IEC standards, the center regions of interest (ROIs) of the water phantoms were selected for the CT number and noise measurements at different dose levels (50/100/200/400 mAs). For the Canon TOS phantom, 5 ROIs at each of the material (water, Delrin, Acryl, 66Nylon, P.P.) were measured for CT numbers and compared with EID measurements. The center and 4 peripheral ROIs of the water phantoms were measured for CT number uniformity assessment.

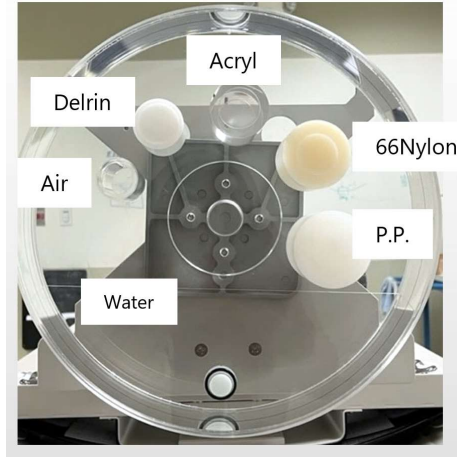


Figure 4: Canon TOS phantom with a diameter of 32cm. It has inserts of different materials for HU accuracy evaluation.

The in-plane spatial resolution was measured using a Catphan CTP682 (The Phantom Laboratory, NY, USA) (Figure 5) scanned at 200 mAs. The radial edge profile of the Teflon pin was used to calculate the Modulation Transfer Function (MTF), and module CTP714 was used for the high contrast line pair phantom measurement for a visual inspection. The same set of phantoms were also used for spectral mode VMI evaluations.

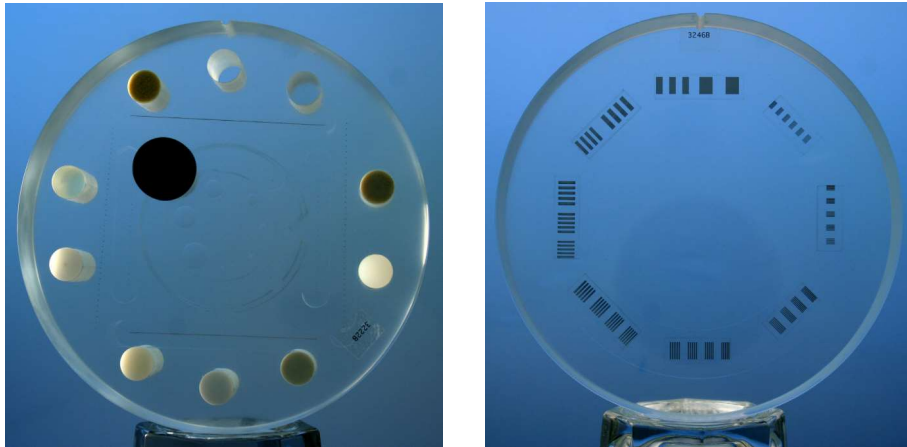


Figure 5: Catphan CTP682 (left) and CTP714 (right) (The Phantom Laboratory, NY, USA) used for image in-plane spatial resolution evaluation.

To examine the spectral material decomposition accuracy, a Multi-energy CT phantom (Sun Nuclear Corporation, WI, USA) was used for evaluations. Iodine inserts with concentration of 2/5/10/15 mg/ml and calcium inserts with concentrations of 50/100/300 mg/ml were placed inside the solid HEwater phantom base.

Both the head-size (20 cm diameter) and body-size (40 cm×30 cm) configurations (Figure 6) were scanned at 4 different dose levels (50/100/200/400 mAs). VMIs at 60 keV and 90 keV were used to extract the iodine and calcium inserts concentrations. In addition, with an appropriate mask, the iodine and calcium maps were generated, and the concentration accuracies were assessed across different dose levels.



Figure 6: Pictures of the Multi-energy CT phantom (head and body size) with different concentrations of iodine/calcium inserts used for quantitative spectral imaging evaluations.

Next, the image CNR was evaluated for both the counting and spectral modes. Both the Multi-energy CT head phantom (Figure 6) and the low contrast sensitivity Catphan module (CTP515) were used for this evaluation. The Catphan scan was acquired at 400mAs, and reconstructed with dFOV 200 mm using a standard body kernel (FC13). The CNR of the different contrast ROIs from the HEwater background ROI were measured. By assuming a linear correlation between the iodine concentration and 50 keV image HU, we matched the projected CNR of different iodine concentrations between PCCT and EID-CT to predict how much iodine contrast agent reduction could be achieved.

3. RESULTS

CT Number Accuracy, Noise and Uniformity

First, a set of water images at different dose levels are displayed in Figure 7. All the images look uniform under a display window of WW/WL=300/0 HU and free of any noticeable artifact. The mean HU and noise as in the ROI standard deviation of the center FOV are displayed in Figure 8. For all the phantom sizes and dose levels, the CT number accuracy is mostly within ± 3 HU. For different phantom sizes, one can observe that the

measured noise-to-dose curves nicely follow the theoretical relationship: $\text{noise} \propto 1/\sqrt{\text{dose}}$ with Poisson statistics. This is a result of effectively removing the electronic noise in the PCD measurement and a good control of pulse pileup effect in the relevant flux range.

The image uniformity measurement results are displayed in Figure 8. The uniformities of the mean HU in the selected 5 ROIs are all within ± 5 HU up to 32 cm water phantom, meeting the typical criteria for clinical diagnosis.

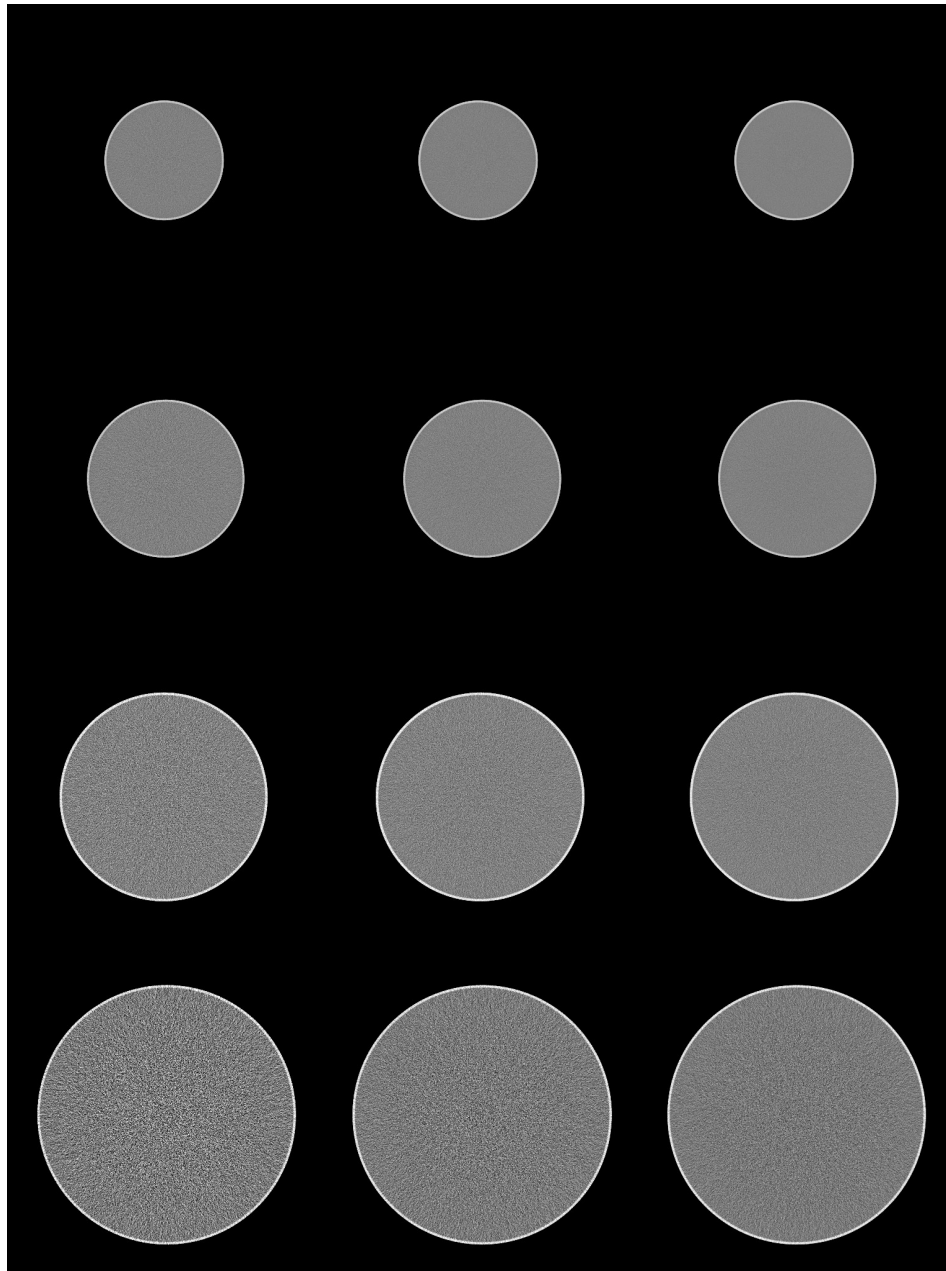


Figure 7: PCCT NR counting images of 4 different sizes of water phantoms, acquired at 120 kVp. From top to bottom are: 18, 24, 32, and 40 cm diameter water phantoms respectively. From left to right columns are with 50, 100, and 200 mAs. The images were reconstructed using FBP with a standard body kernel (FC13) with 500 mm FOV, and displayed with 5 mm slice thickness at WW/WL = 300/0 HU.

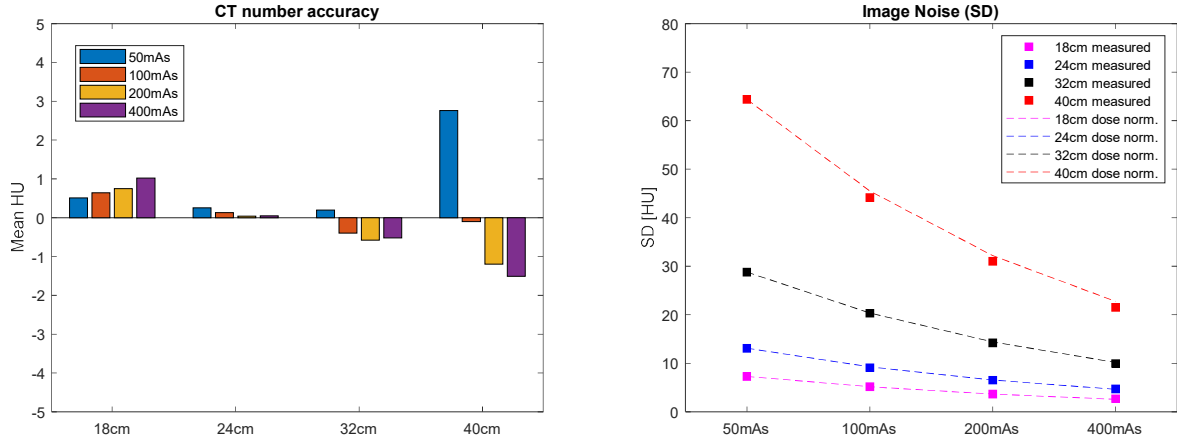


Figure 8: (left) CT number (HU) and noise standard deviation (SD) measurement from the center ROI of the PCCT water images. Most of the measurements are well within ± 3 HU across the phantom sizes and dose levels, indicating good calibration quality. (right) Image noises decrease linearly with $1/\sqrt{\text{dose}}$ (dashed lines), indicating little influence from electrical noise at low dose condition and pulse pileup at a high dose condition.

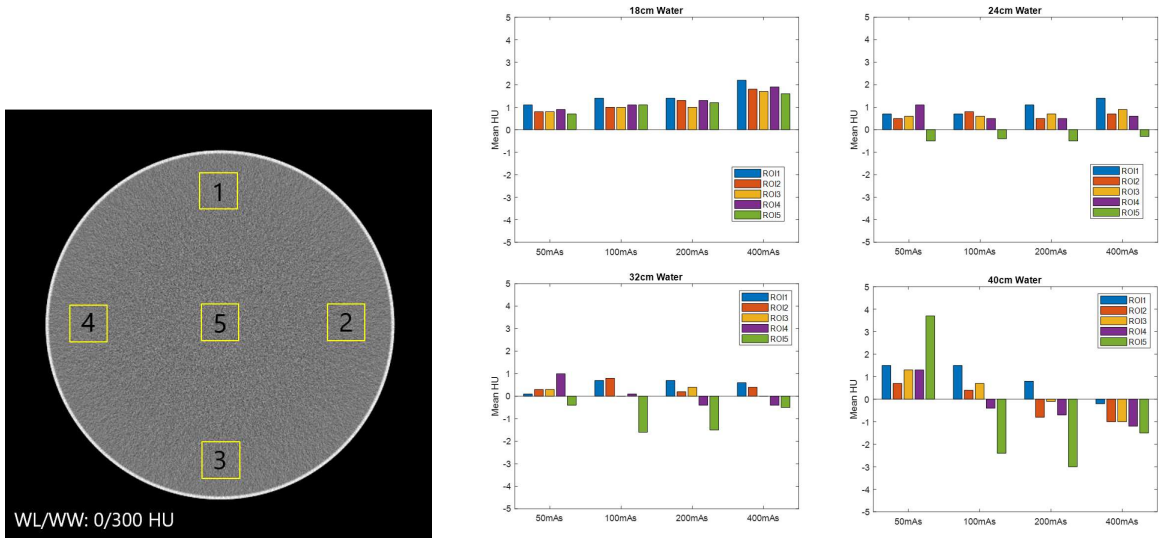


Figure 9: 5 ROIs (see left figure) were selected from the center and the peripheral of water images (400 mAs, 40 cm water phantom, 5 mm slice thickness) for the CT number uniformity measurement. For all phantom sizes and dose levels, the uniformity is well within ± 5 HU.

We also evaluated the Canon TOS phantom which has multiple different contrasts, and the results are shown in Figure 10 and Table 2. The mean CT numbers of the 5 ROIs from PCCT images match well with typical

EID-CT measurement range. Results at all 4 dose levels also have good consistency with maximum deviations within ± 1 HU.

Table 2: Canon TOS phantom mean HU measurements from PCCT and EID-CT. The CT numbers of all 5 ROIs from PCCT images over all 4 dose levels match well with EID-CT measurement.

ROI#	EID Ref. HU	PCCT HU (mean)
(1) Water	0 ± 5	-0.175
(2) Delrin	340 ± 10	333.6
(3) Acryl	130 ± 10	123.0
(4) 66Nylon	100 ± 10	92.7
(5) P.P.	-105 ± 10	-108.6

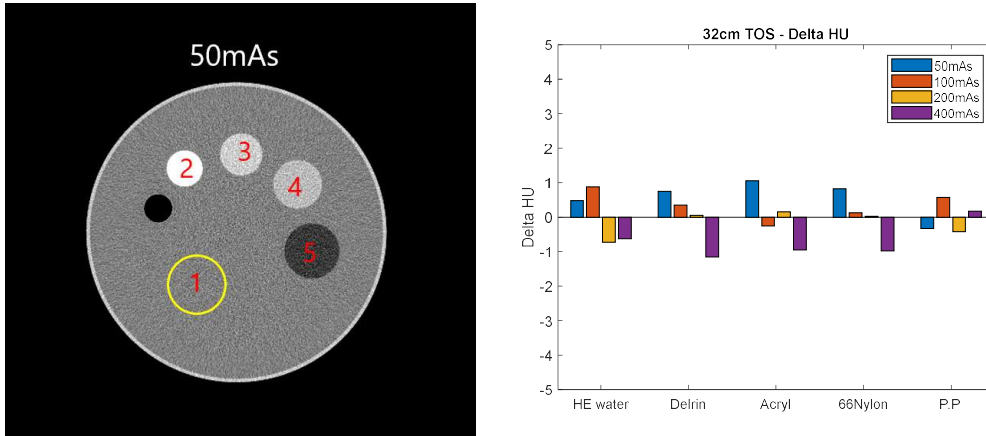


Figure 10: CT number measurements in a Canon TOS phantom PCCT image. All 5 ROIs selected at different materials have good HU consistency across the dose levels, indicating little influence from electronic noise nor the pulse pileup effect.

The in-plane spatial resolution of the normal resolution (NR) mode images was measured using the high contrast Teflon pin in Catphan CTP682 (Figure 11). With a large focal spot size and a standard body reconstruction kernel (FC13), the 50% modulation transfer function (MTF) is 0.33 lp/mm and the 10% MTF is 0.69 lp/mm. Compared with EID-CT using the same scanning condition and reconstruction kernel, PCCT produces 15% improvement of the MTF as shown in Figure 11. A visual comparison that demonstrates the PCCT in-plane spatial resolution improvement is also shown in Figure 12. The Multi-energy CT head phantom

was scanned at 400 mAs for both EID-CT and PCCT NR mode, and the PCCT image clearly shows better edge definition around the air gap and the inserts.

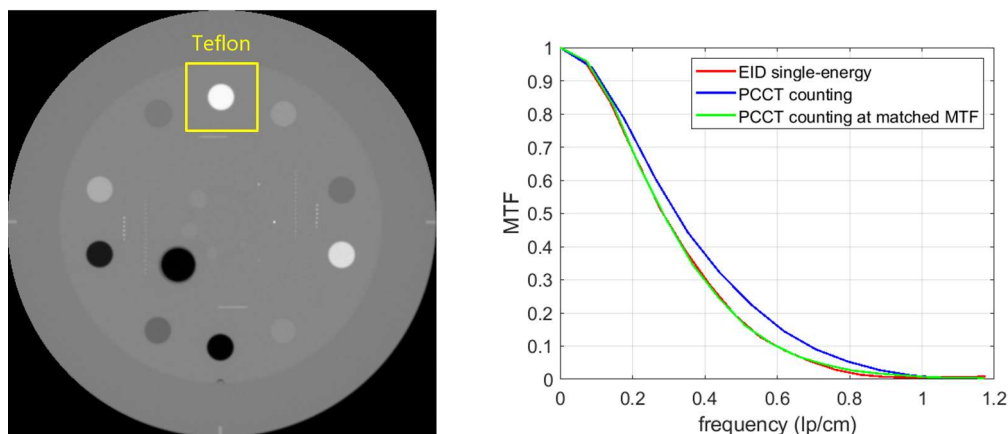


Figure 11: (Left) PCCT NR counting image of Catphan CTP682, acquired with large focal spot at 400 mAs and reconstructed by a standard body kernel (FC13). The radial edge profile of the Teflon pin was used for the MTF measurement. (Right) For PCCT counting, the 50% MTF is 0.33 lp/mm and the 10% MTF is 0.69 lp/mm, which is higher than EID-CT (0.30 lp/mm at 50% MTF and 0.60 lp/mm at 10% MTF.) With additional smoothing on the PCCT image, the MTF can be matched with the EID-CT for noise comparison.

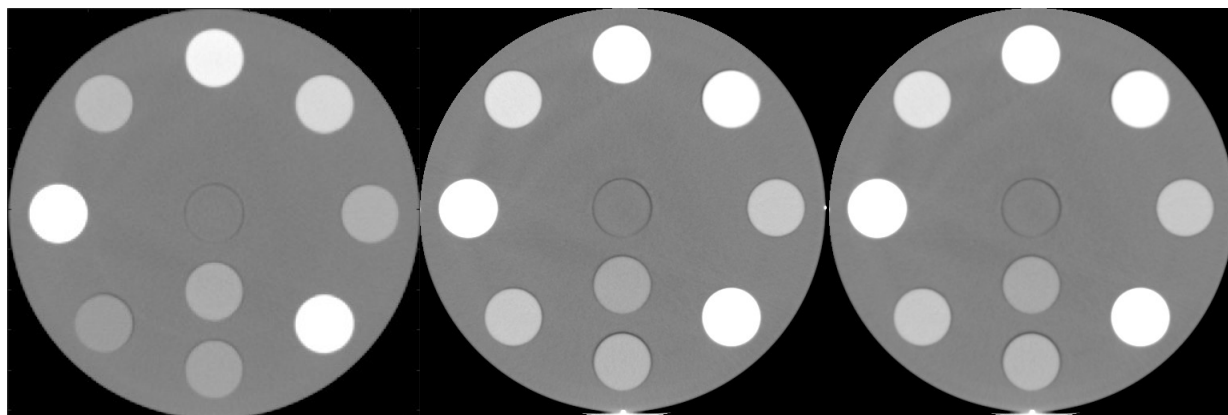


Figure 12: Multi-energy CT head phantom images acquired from EID-CT (left) and PCCT (middle and right) at 400 mAs and displayed at WW/WL: 400/0 HU. With the same large focal spot size, beam filtration and matched radiation dose, the PCCT NR counting image clearly shows the spatial resolution improvement around the air gaps of inserts. The MTF matched PCCT image shows similar sharpness as the EID-CT image with reduced noise.

To further demonstrate the potential benefit of PCCT, we compared the image noise by applying additional smoothing on the PCCT data to match the EID-CT MTF. This was achieved by applying a carefully tuned 2-D

Gaussian filter on the PCCT sinogram data. The matched MTFs are shown in Figure 11. Next, we compare the image noise of the 40 cm water phantom between PCCT and EID-CT (Figure 13). Without MTF matching, PCCT NR counting images have lower noise than EID-CT images at lower dose levels. The noise reduction is more significant as dose decreases. After matching MTF, the PCCT images show significant noise reduction for all dose levels, up to 53% at 50 mAs (Figure 14), which is equivalent to a 72% dose reduction for getting the same image noise as EID-CT.

Another observation at the 50 mAs 40 cm water phantom case is that, the PCCT image has improved uniformity, while the EID-CT image has noticeable bias towards the image center. We believe that the improvement of both the noise and bias is largely attributed to the reduced influence of electronic noise in PCCT. The noise grain of the PCCT image is also finer, indicating that the noise power spectrum shifts toward higher frequency.

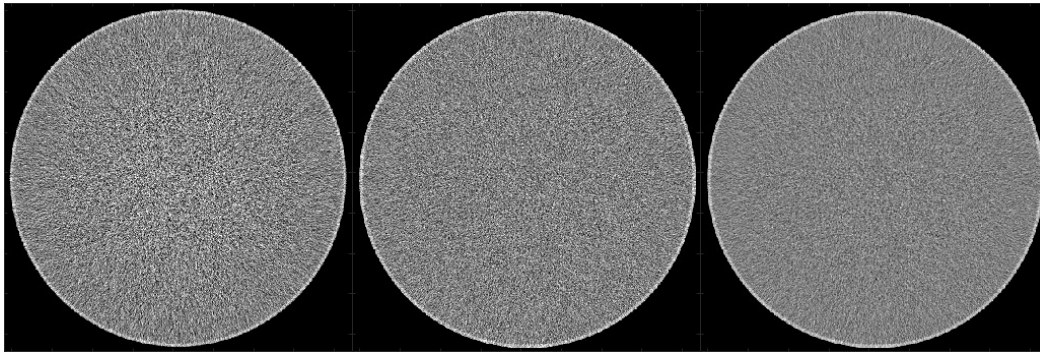


Figure 13: Images of a 40 cm water phantom acquired at 120 kVp, 50 mAs from EID-CT (left) and PCCT (middle & right) with a display window of WW/WL: 400/0 HU. Middle image is from PCCT, and right image is from PCCT with additional denoising to match the EID-CT image MTF. The PCCT images show improved uniformity over the entire phantom while the EID-CT has noticeable HU bias towards the center. The noise in the MTF matched PCCT image is significantly reduced compared to the EID-CT image.

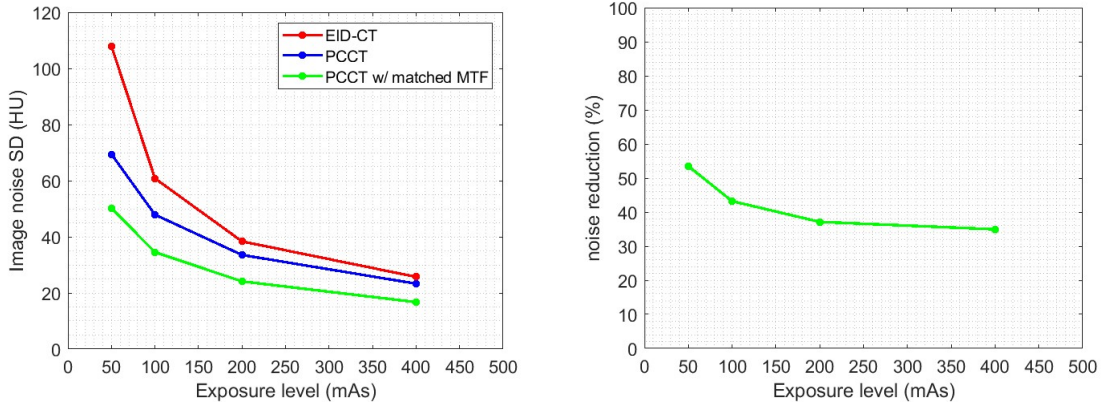


Figure 14: Noise standard deviation (SD) on a 40 cm water phantom from 50 mAs to 400 mAs, measured using a 16 cm diameter ROI placed at the center. Compared to EID-CT images, PCCT has reduced noise at low dose levels and obtained similar noise level at high dose levels. After MTF matching with EID-CT, PCCT images show much greater noise reduction across all dose levels.

Spectral VMI, material quantification, CNR

The basic image quality was also evaluated for the PCCT VMIs generated from spectral mode. Examples of a 24 cm water phantom keV images are shown in Figure 15. The quantitative measurement in Table 3 shows that from low to high keV, VMIs have similar HU uniformity as the counting image. In particular, the 70 keV image has very similar noise level as the counting image. The mean HU number of the center ROI and the HU standard deviation were measured to assess the 70 keV VMI HU accuracy for different sizes of water phantoms (Figure 16). For all the phantom sizes, the 70 keV VMI has similar HU accuracy and noise as the counting image.

The in-plane spatial resolution of PCCT VMIs was also assessed and compared with PCCT NR counting and EID-CT rotate-rotate DE VMIs (Figure 17). The results show that 1) PCCT VMIs demonstrate an MTF as consistent with the PCCT NR counting image; 2) PCCT VMI has an MTF superior to the EID-CT rotate-rotate DE image at 50 keV.

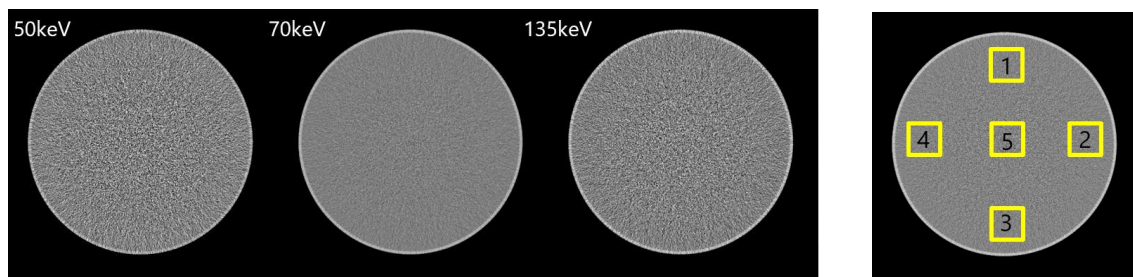


Figure 15: PCCT NR VMIs (left) and counting image (right) for a 24 cm water phantom scanned at 100 mAs, 0.62 mm slice thickness with display window WW/WL: 400/0 HU. The 70 keV image has very similar noise level as the counting image (right). The 5 ROIs selected for HU uniformity measurement are displayed on the counting image on the right.

Table 3: HU uniformity measurement for 24 cm water phantom PCCT VMIs.

	ROI1	ROI2	ROI3	ROI4	ROI5	Max Δ HU
Counting	1.1	1.2	0.8	0.8	1.0	1.2
50 keV	2.9	3.8	1.9	4.2	-1.5	5.7
70 keV	-2.6	-1.2	-2.2	-2.0	-2.4	1.4
135 keV	-0.8	0.3	0.3	-0.6	2.4	3.2

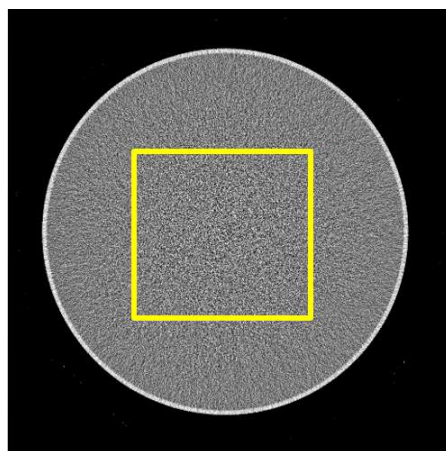


Figure 16: PCCT 70 keV VMI of a 32 cm water phantom scanned at 100 mAs, 0.62 mm slice thickness and displayed at WW/WL: 400/0. The center ROI was selected for the HU accuracy and noise comparison with NR counting images.

Table 4: PCCT NR counting and 70 keV VMI HU accuracy and noise comparison for different sizes of water phantoms. The 70 keV VMI has similar performance as the counting image.

Center ROI Mean/SD	Water 18 cm	Water 24 cm	Water 32 cm
Counting	-0.1/15.9	0.2/28.19	0.2/60.6
70 keV	-0.5/17.6	-2.6/29.4	0.1/63.3

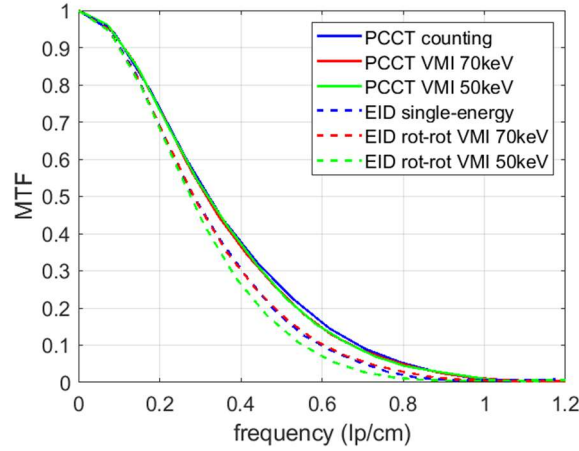


Figure 17: PCCT VMIs has an MTF consistent with the PCCT counting image, which is superior to that of EID-CT single-energy and DE mode VMIs using 80/135 kVp.

Compared to the counting image, one advantage of the VMIs is that the beam hardening artifact can be mostly removed given an accurate material decomposition. This is demonstrated in Figure 18 that a 70 keV VMI shows a further reduced beam hardening artifact compared with the counting image of the Multi-energy CT head phantom. The minor shading between the high contrast rods in the counting image is further diminished in the 70 keV VMI. To quantify this improvement, the maximum HU deviation of the neighboring ROIs was measured. The counting image has a 5.4 HU deviation while the 70 keV VMI has only 1.3 HU (Table 5).

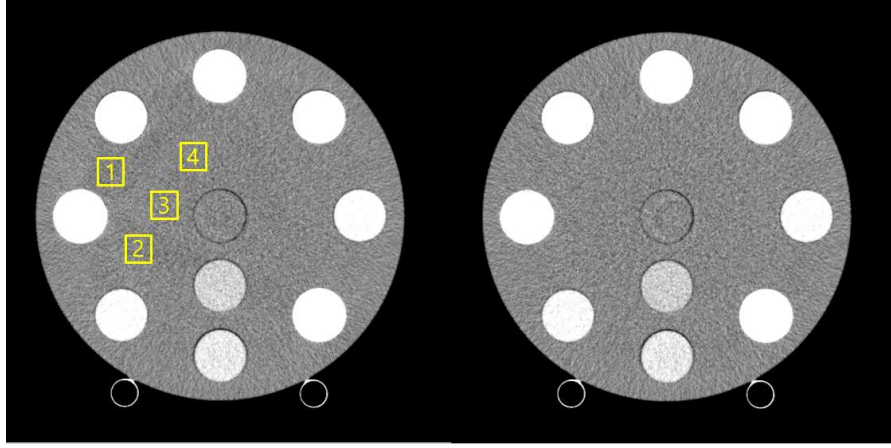


Figure 18: PCCT NR counting and 70keV VMI of the Multi-energy CT head phantom scanned at 100 mAs, 5mm slice thickness displayed at WW/WL:200/0 HU. 4 different small ROIs around the high contrast rods were selected to quantitatively assess the residual beam hardening artifact.

Table 5: Mean CT number within selected ROIs and maximum deviation for PCCT counting and 70 keV VMI of the Multi-energy CT head phantom. With highly attenuated rods, 70 keV VMI shows further improved CT number uniformity in the whole image than the counting mode due to reduced beam hardening artifact.

	Average CT number within ROI (HU)				Max. Δ HU
	ROI1	ROI2	ROI3	ROI4	
Counting	0.2	-0.1	5.3	2.4	5.4
70keV VMI	-2.8	-3.3	-4.1	-3.7	1.3

By using the HU values in two different keV VMIs (e.g., 60 keV & 90 keV), one can classify different materials that may not be distinguishable in the conventional EID-CT image or the PCCT counting image and quantify their material concentrations with a known composition. A set of example VMIs of Multi-energy CT head phantom and the projected material maps are shown in Figure 19. We evaluated both the iodine and calcium rods concentration in the Multi-energy CT head phantom for all dose levels. The results are summarized in Table 6 and Table 7. Both iodine and calcium rods concentrations were estimated accurately for all concentration levels.

As previously demonstrated that the PCCT NR image has superior in-plane resolution than EID-CT, we first apply the same Gaussian filter to the PCCT monoenergetic sinogram data to match the 70 keV VMI and EID-CT 70 keV VMI MTF, then compare the noise performance of PCCT VMIs with the EID-CT VMIs with and without the MTF matching. As plotted in Figure 21, the original PCCT VMIs have lower noise across the whole energy range, and by trading off that additional spatial resolution, the noise is further reduced. Another

observation is that the lowest noise of PCCT VMIs is in the vicinity of 65 keV for this phantom, and is consistent with the counting image noise. This can be expected since the same photon statistics are used for both counting and spectral mode processing, and could indicate that little additional noise is introduced during the PCCT material decomposition step.

With the improved noise and MTF in VMIs, we compare the material quantification results between PCCT at 100 mAs and EID-CT rotate-rotate DE at matched dose level (Table 8). The overall quantification accuracy of PCCT is improved for all concentrations with significantly reduced noise.

As a result of more optimal photon weighting and reduced noise in PCCT, the image CNR is improved (Figure 20). For the PCCT NR counting mode, the original images show higher CNR than EID-CT for all the evaluated iodine and calcium concentrations. The MTF-matched images show additional improvement due to further reduced image noise. For VMIs, in particular from 40 keV to 70 keV, PCCT also produces consistently higher CNR than EID-CT, with on average a 56% improvement and a minimum of 26% improvement (2 mg/ml at 55 keV) (Figure 21). One thing to note is that, even with matched 70 keV VMI resolution, the PCCT 50 keV VMI still has superior resolution than EID-CT (Figure 13), providing room for further noise-resolution trade-off to optimize the low keV VMI diagnosis capability.

By assuming a linear correlation between the contrast concentration and the VMI HU number, with the four different iodine concentration inserts HU values in 50 keV VMIs, we calculated the projected CNR curve vs. iodine concentrations for PCCT and EID-CT. With the same CNR for both PCCT and EID-CT, we estimated how much iodine concentration reduction can be achieved for PCCT. As shown in Figure 22, from 2 mg/ml to 15 mg/ml, to achieve the same CNR, an average of ~32% less iodine concentration can be used for PCCT.

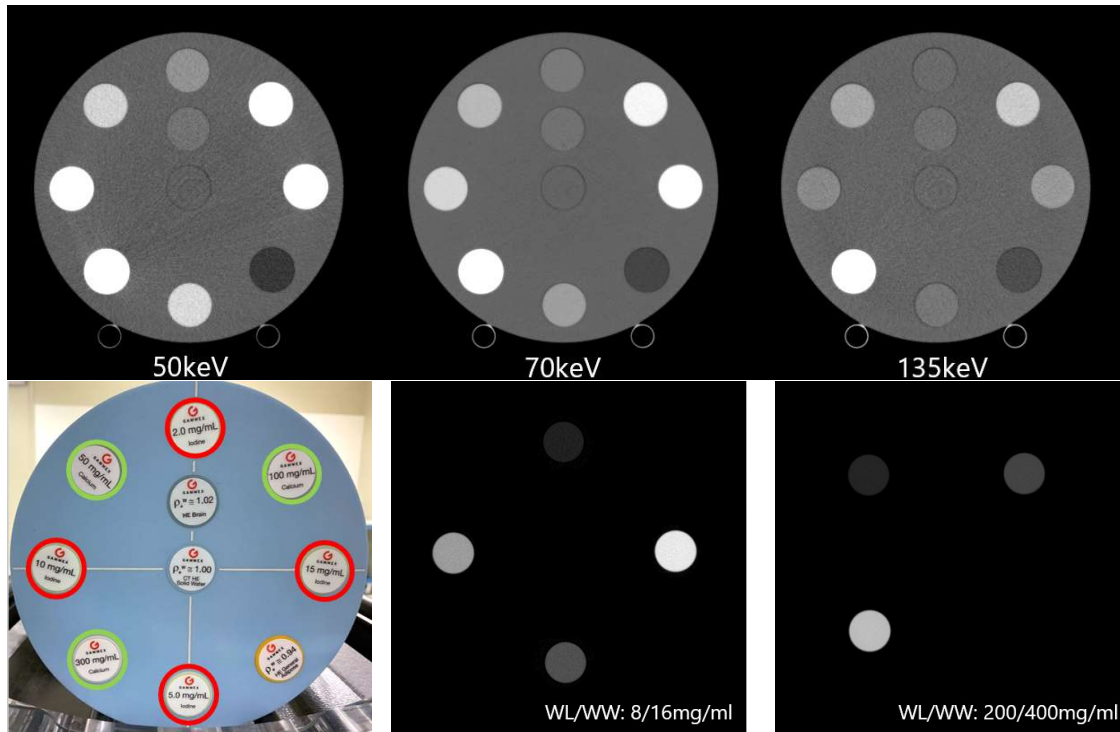


Figure 19: (Top) Multi-energy CT head phantom VMIs from PCCT scanned at 200 mAs, and displayed with 5 mm slice thickness at window WW/WL:600/60 HU. (Bottom) The picture of the phantom inserts arrangement (left). Projected iodine (middle) and calcium (right) maps using VMIs match well with the ground truth phantom configuration.

Table 6: Measured iodine concentrations using PCCT VMIs for the Multi-energy CT head phantom. The measurements were made on the 5 mm slice thickness images at 4 different dose levels. The root-mean-square-error (RMSE) for each level of concentration was also calculated.

Ground truth Iodine concentration (mg/ml)	PCCT measured mean and SD (mg/ml)			
	500 mAs	100 mAs	200 mAs	400 mAs
2	2.02±0.29	2.01±0.21	2.03±0.14	2.09±0.11
5	5.07±0.32	5.04±0.21	5.04±0.15	5.11±0.12
10	9.91±0.30	9.85±0.23	9.80±0.16	9.90±0.13
15	14.85±0.34	14.76±0.23	14.61±0.19	14.76±0.14
RMSE	0.084	0.14	0.22	0.15

Table 7: Measured calcium concentrations using PCCT VMIs for the Multi-energy CT head phantom. The measurements were made on the 5 mm slice thickness images at 4 different dose levels. The RMSE for each level of concentration was also calculated.

Ground truth Calcium concentration (mg/ml)	PCCT measured mean and SD (mg/ml)			
	500 mAs	100 mAs	200 mAs	400 mAs
50	57.69±2.87	57.57±2.08	57.63±1.46	58.00±1.15
100	106.88±3.12	106.57±2.20	106.43±1.63	107.01±1.23
300	302.58±3.95	301.14±3.00	297.50±1.95	298.80±1.46
RMSE	6.14	5.82	5.94	6.18

Table 8: Iodine concentration accuracy compared between PCCT and EID-CT using 100 mAs scans on the Multi-energy CT head phantom. The measured concentration values were extracted from the 60 keV and 90 keV VMIs using the theoretical HU value of the materials as reference. The results show that PCCT has improved iodine quantification accuracy and noise as compared to the EID-CT system with matched 70 keV VMI MTF.

Ground Truth iodine concentration (mg/mL)	PCCT measured value (mg/mL)	EID-CT measured value (mg/mL)
2	2.01±0.15	1.83±0.27
5	5.05±0.15	4.33±0.25
10	9.85±0.17	9.27±0.23
15	14.77±0.17	14.22±0.25

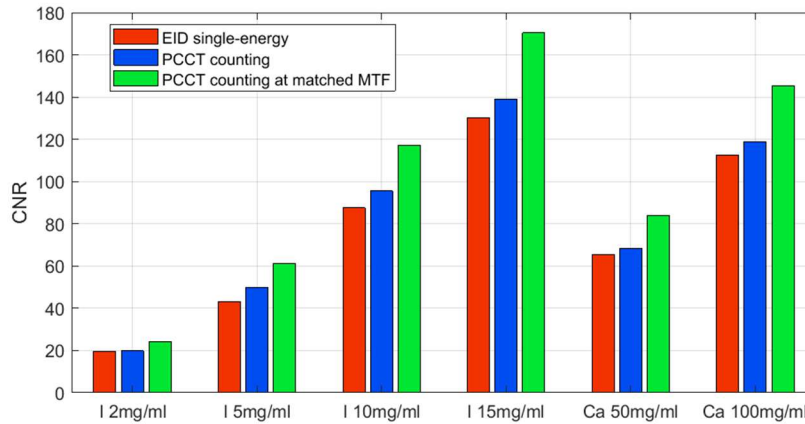


Figure 20: CNR comparison among EID-CT single-energy, PCCT counting, and PCCT counting at matched MTF with EID-CT. Both the original PCCT counting and MTF-matched PCCT counting present higher CNR than EID single-energy CT in iodine and calcium objects across multiple concentrations. The average CNR improvement over EID-CT single-energy is 7% for original PCCT counting and 31% for MTF-matched PCCT counting.

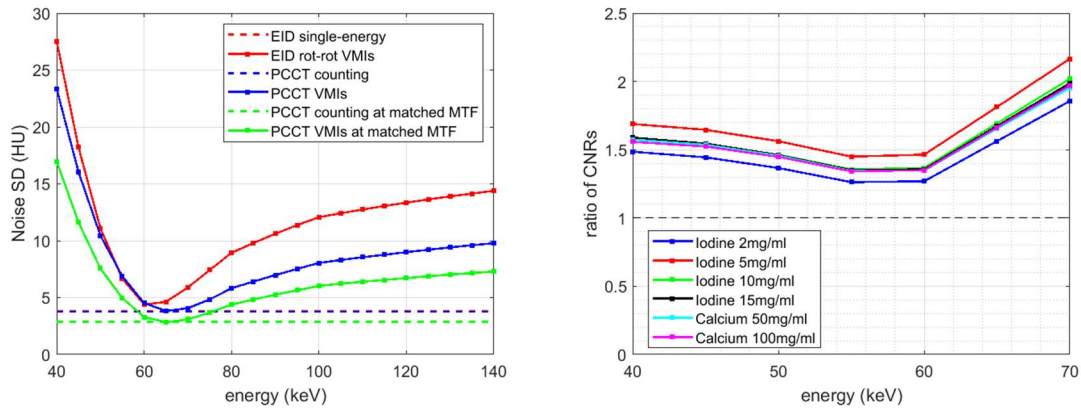


Figure 21: (Left) Image noise comparison shows that PCCT VMIs with matched MTF with EID-CT 70 keV VMI present much lower noise than EID-CT VMIs, with noise measured at the phantom base material. (Right) Ratio of resolution-matched PCCT VMI CNR to EID-CT VMI CNR. With matched resolution at 70 keV VMI, PCCT VMIs have consistently higher CNR than EID-CT VMIs across all energies for all contrast objects, with 56% CNR improvement on average within the range of 40 keV to 70 keV and a minimum of 26% CNR improvement (2 mg/ml iodine at 55 keV).

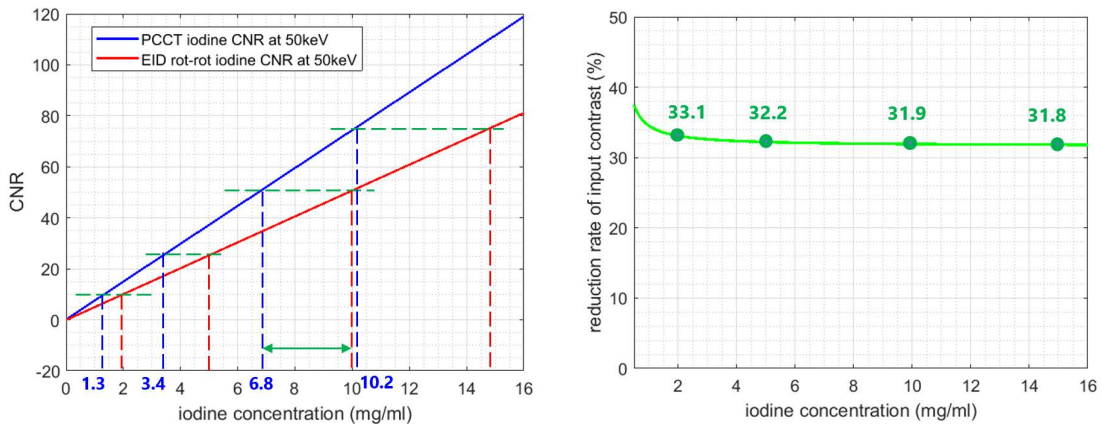


Figure 22: (left) Projected iodine CNR from the solid-water background with different iodine concentrations in mg/ml. For all the concentration levels, PCCT has significantly less projected contrast concentration to achieve the same CNR at 50 keV VMI as measured in EID-CT and can potentially save 32% iodine contrast usage in clinical settings for concentration level between 2 mg/ml to 15 mg/ml on average.

The CNR improvement is also assessed on low contrast Catphan CTP515. The PCCT NR counting and EID-CT images are displayed in Figure 23. The images were acquired with 400 mAs and reconstructed with 5mm thickness using the same standard body recon kernel (FC13). The PCCT original image has better edge

definition for all the low contrast supra-slices and subslices, and visually allows one to better identify smaller objects with lower contrast from the background. Two small ROIs were selected at the 15mm diameter target of 1.0% supra-slice region and the background to calculate the CNR. The results are summarized in Table 9. With matched MTF, the PCCT image increases the low contrast CNR from 2.5 to 4.6, a ~84% improvement over EID-CT.

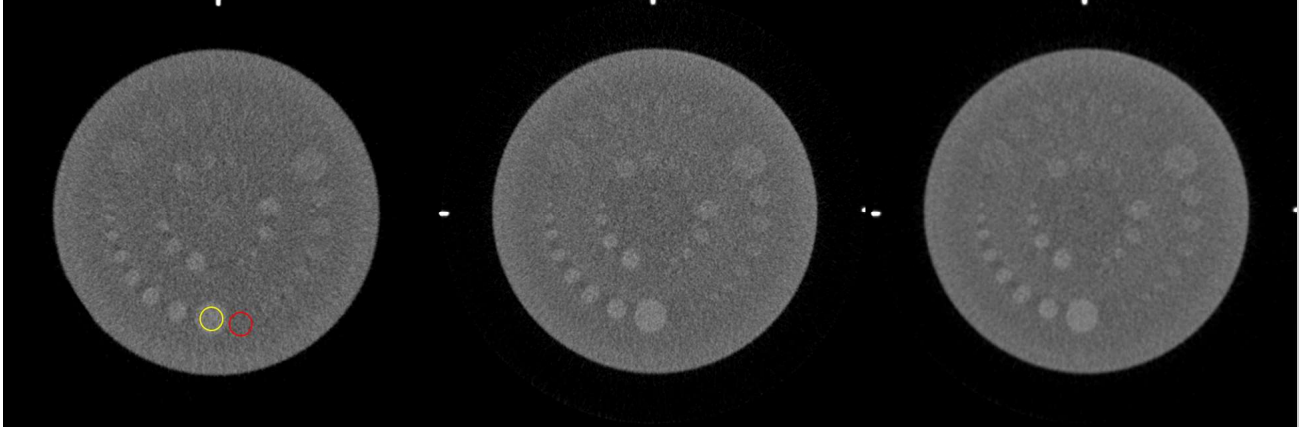


Figure 23: Images of low contrast Catphan CTP515 from EID-CT and PCCT. Scans were acquired with 400 mAs and reconstructed with a standard body kernel (FC13). Display window: WW/WL=100/60 HU. Left is EID-CT image with 2 selected ROIs to evaluate the NCR at the 15 mm diameter target of the 1% supra-slice contrast level. Middle is the PCCT original image, and right is the PCCT image with matched MTF with EID-CT image. The improved spatial resolution in the PCCT image provides better edge definition for those low contrast inserts, hence could increase the detectability of such low contrast objects. Even with a simple Gaussian denoising, the MTF-matched PCCT image allows for better identification of smaller inserts.

Table 9: Low contrast object CNR comparison between PCCT and EID-CT using Catphan CTP515. CNR of the 15 mm diameter target at 1.0% contrast level increases from 2.5 in EID-CT to 4.6 in PCCT with matched-image MTF.

	ViSION	PCCT	PCCT w/ matched MTF
Object	60.2±3.6 HU	58.5±3.2 HU	58.5±1.8 HU
Background	50.6±3.9 HU	48.3±3.9 HU	48.3±2.2 HU
Contrast	9.6	10.2	10.2
CNR	2.5	2.6	4.6

As previously studied in the literature [26][27], the material decomposition noise is reduced with more energy bins due to better spectral resolution and is one major benefit of PCCT with multi-energy bin measurements. Comparing to the image-based material decomposition approach, which requires reconstruction of individual

energy bin images in the first place and is more prone to the beam hardening artifacts and detector response modeling errors when energy bins get finer [9][26], one advantage of using projection domain decomposition is to handle multiple energy bin data more coherently, hence more resilient to the modeling errors in each energy bin. As an example, we compare the Multi-energy CT head phantom images generated from 2-energy bin data (30/65 keV) vs. 5-energy bin data (30/45/55/65/80 keV). From visual inspection, both 50 keV VMIs have good image quality in general, with the 2-energy bin decomposition image shows elevated noise (Figure 24). We selected one of the inserts for quantitative comparison. The noise SD on of the selected ROI was measured in 50/70/135 keV VMIs for both cases, and the results are listed in Table 10. VMIs with 2 energy-bin material decomposition have 20.5 to 24.5% higher noise for this tested case.

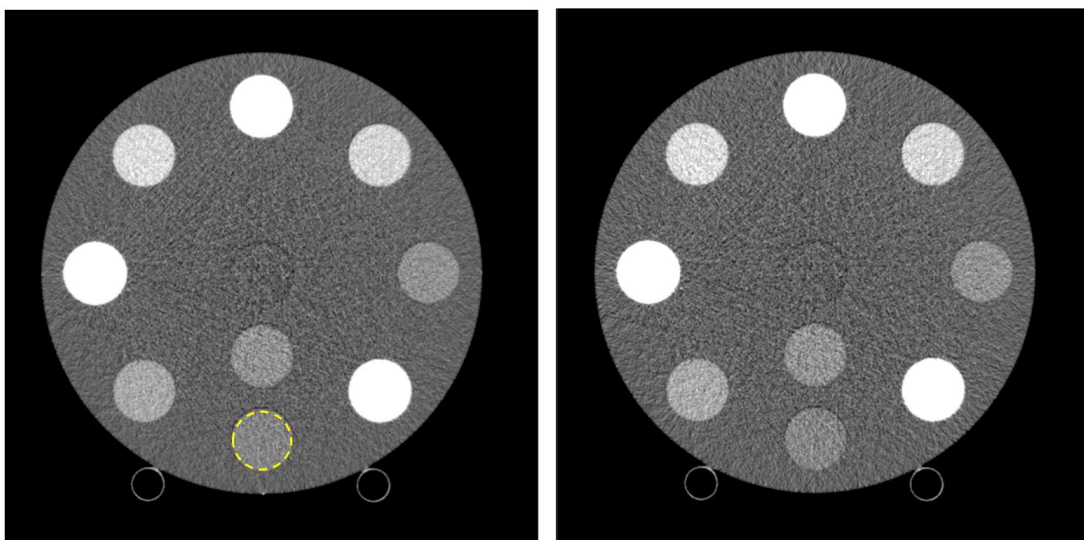


Figure 24: PCCT 50 keV VMIs using 5-energy bin decomposition (left) vs. 2-energy bin decomposition (right) from the Multi-energy CT head phantom. The scan was acquired at 200mAs, and reconstructed with a standard body kernel (FC13) at 0.62 mm slice thickness. The 5 energy bin data was recombined into 2 energy bins (30/65 keV) for generating another set of spectral images. The images are displayed at WW/WL: 600/60 HU. The overall image quality looks similar between the two, and the 2-bin decomposition image shows increased image noise. An ROI at the phantom edge was selected for quantitative noise comparison.

Table 10: PCCT VMI noise with different energy bin data input for material decomposition from a 200 mAs Multi-energy CT head phantom scan. The same scan data was processed differently, one with the original 5-bin data and another with recombined 2-bin data. For all the reconstructed VMIs, 2-bin decomposition generates high noise in the image.

Material decomposition input	50 keV SD	70 keV SD	135 keV SD
5-bin (30/45/55/65/80 keV)	33.1	11.2	28.0
2-bin (30/65 keV)	41.2	13.5	34.2
Noise increased in 2-bin decomposition	24.5%	20.5%	22.0%

Super high-resolution

The PCCT system also allows for SHR imaging using the micro-pixel level readout for reconstruction. The NR counting and SHR counting images of the high-contrast line pair Catphan CTP714 are displayed in Figure 25. The phantom was scanned at 200 mAs with a small focal spot size. The image was reconstructed with a standard body kernel (FC13). The 9 lp/cm bars can be visually identified in the NR image while at least 15 lp/cm pair can be identified in the SHR image. The MTF measurement using the same standard body kernel (FC13) of NR and SHR mode is displayed in Figure 26. At least a 91% improvement by SHR mode at 10% MTF is observed from the MTF curves. Although these results are still preliminary and do not represent the best SHR performance due to the relatively large focal size and suboptimal reconstruction kernel, the improvement of the spatial resolution is clearly demonstrated in the LUNGMAN phantom (Kyoto Kagaku Co. Ltd., Japan) images in Figure 27. The SHR phantom image is much sharper visually and reveals more details of the structure.

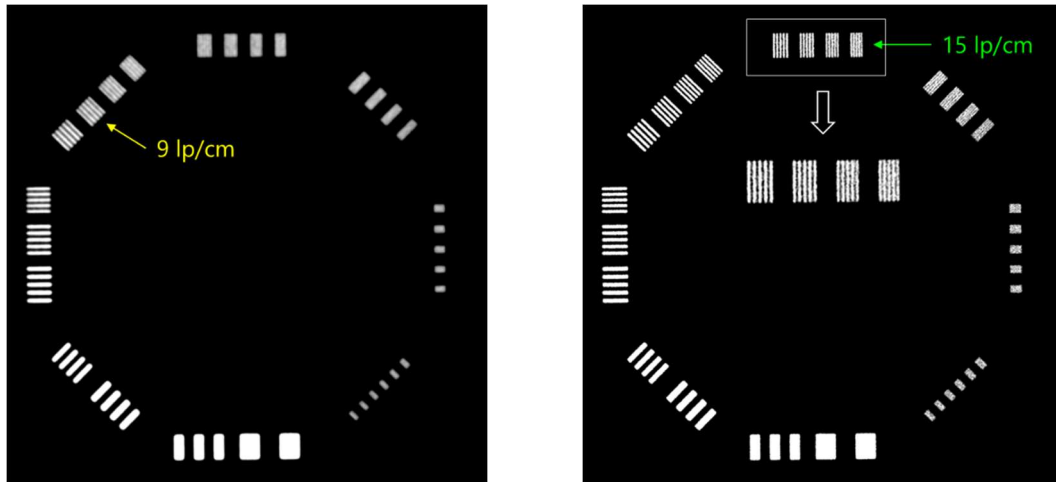


Figure 25: High contrast resolution bars at Catphan CTP714, PCCT NR (left) and SHR (right) images reconstructed with a standard body kernel (FC13). A significant resolution improvement can be observed in SHR mode. Display window: [600 1400] HU.

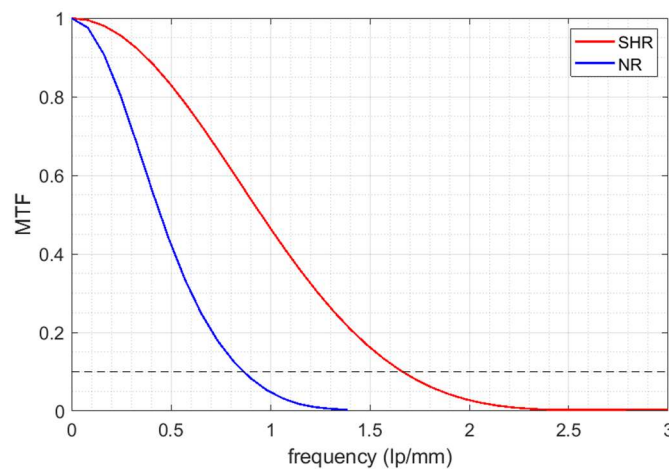


Figure 26: MTF measurement using the Teflon pin in Catphan CTP682 for PCCT NR and SHR mode. Data was acquired at 200 mAs with a small focal spot. Images were reconstructed at 30 mm dFOV using a standard body kernel (FC13). The MTF result shows that the PCCT SHR image has a 91% boost at 10% MTF over the NR image (1.65 lp/mm for SHR vs. 0.86 lp/mm for NR).

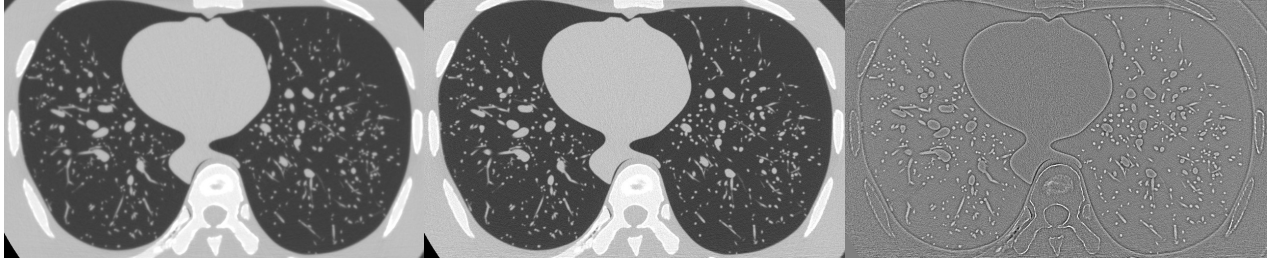


Figure 27: LUNGMAN phantom images of PCCT NR (left) and SHR (middle) counting modes and the corresponding difference image (right). The scan was acquired at 200 mAs and reconstructed using a standard body kernel (FC13) at 0.62 mm slice thickness. Display window for NR/SHR image: [-1500 500] HU, for difference image: [-400 400] HU. No additional image denoising was applied.

4. DISCUSSION AND SUMMARY

In this work, we introduced our first prototype full field-of-view photon counting CT system and evaluated its imaging performance through phantom studies. By comparing with EID-CT performance in the same tasks, we demonstrated that the prototype system is capable of producing diagnostic quality images at all assessed clinical dose levels with superior performance in the following aspects:

1. PCCT significantly reduces image noise, particularly in low dose cases. This is mainly due to the removal of electronic noise in the counting mode with an appropriate energy threshold. We observed up to 37% noise reduced in a 40 cm water phantom counting image with the same scan settings as EID-CT at 50 mAs, and at different dose levels, the noise nicely follows Poisson statistics. Another associated benefit is fewer image artifacts from photon starvation, which potentially allows for lower dose to achieve the same image quality in a clinical setting.
2. PCCT improves image spatial resolution. With the same in-plane detection pitch as the EID-CT, PCCT NR mode still demonstrate better MTF. We observed a $\sim 15\%$ increase in 10% MTF compared to EID-CT which is mainly due to the reduced crosstalk between neighboring pixels. In PCCT, the crosstalk effect is mainly from the charge-sharing effect, and is mostly confined between neighboring micro-pixels [29]. While for EID-CT, due to the two-stage conversion process, the crosstalk kernel is at least at the width of a macro-pixel with larger magnitude. PCCT can also have more flexible readout modes, from the current '3 \times 3' grid to other types of summing grids to further optimize the NR mode resolution. With improved spatial resolution, it provides more room for trade-off when applying denoising to optimize the image quality depending on the tasks. As an example, our results demonstrated that up to 53% noise reduction can be achieved by simply matching the MTF with EID-CT for a 40 cm water phantom at 50mAs, which is equivalent to a 72% dose reduction.

3. PCCT can produce SHR images from the micro-pixel level readout. With only roughly 1/9 of the conventional detector pixel size, the limiting resolution is largely increased and images are much sharper and can reveal many more details. We observed a 91% increase in 10% MTF from the NR to SHR with a standard body recon kernel (FC13), and it is yet the full potential of the current PCCT due to the relatively large focal spot size and suboptimal reconstruction kernel.
4. PCCT can enable spectral imaging without introducing additional complications from workflow or data temporal inconsistency like conventional DECT using dual source or fast kVp switching. Using a projection domain decomposition approach, it can flexibly utilize multiple (≥ 2) energy bin input with more spectral information and further reduce spectral image noise. We have demonstrated that the VMIs generated with 5-energy bin data have significantly lower image noise across all keVs than the 2-energy bin data which is consistent with previous estimates. It is demonstrated that PCCT VMIs using 5-energy bins have better quantitative accuracy and much lower noise than EID rotate-rotate DECT. The resulting material quantification has excellent accuracy and uncertainty with a mean RSME of 0.15 mg/ml and 6.02 mg/ml for iodine and calcium, respectively. It is also demonstrated that PCCT VMIs further reduce beam hardening artifacts and preserve the same spatial resolution as the counting mode. These findings may open new opportunities in spectral imaging applications.
5. PCCT registers each photon equally, and together with the reduced noise, PCCT can generate better CNR in different tasks. As we evaluated through this work, in both high contrast and low contrast cases, PCCT demonstrated superior performance in CNR for both counting and spectral modes and can potentially reduce the iodine contrast by 32% while maintaining the same CNR for diagnosis.

There are some limitations in our study. The current prototype system covers up to about 1 cm in Z at isocenter and only supports circular scans at 1 second per rotation. It does not support real time data processing and reconstruction, and cannot conduct more complex scan series to fully mimic clinical workflows. It is also not equipped with high precision tube with smaller focal spot to fully demonstrate the SHR mode spatial resolution capability, or more advanced features such as tube current modulation (AEC) and AI-based denoising for additional dose saving and image quality enhancement. These limitations are mostly engineering related and will be gradually resolved in our future clinical prototypes.

In conclusion, we performed comprehensive phantom imaging evaluations on our first CdZnTe-based prototype PCCT system. Through rigorously designed experiments and analysis, the initial results demonstrate multiple advantages over conventional EID-CT and provide us in-depth understanding of the current PCD performance

under clinical scan conditions and invaluable insights on design trade-offs. Currently, a new generation of clinical prototype PCCT system is under development. With a wider Z coverage, a high precision X-ray tube, faster rotation speeds and improved scan workflows, it will enable patient studies to further demonstrate the clinical values with photon counting detection technology.

REFERENCES

- [1] Taguchi, K., Iwanczyk, JS. Vision 20/20: single photon counting x-ray detectors in medical imaging. *Med Phys* 2013;40(10):100901.
- [2] Kappler, S., Henning, A., Kreisler, B., Schoeck, F., Stierstorfer, K., Flohr, T. Photon counting CT at elevated x-ray tube currents: contrast stability, image noise and multi-energy performance. *Proc. of SPIE: medical imaging 2014, physics of medical imaging*. Vol 9033.
- [3] Persson, M., Huber, B., Karlsson, S., et al. Energy-resolved CT imaging with a photon-counting silicon-strip detector. *Phys Med Biol* 2014;59(22):6709–6727.
- [4] Gutjahr, R., Halaweish, AF., Yu, Z., et al. Human imaging with photon counting based computed tomography at clinical dose levels: contrast-to-noise ratio and cadaver studies. *Invest Radiol* 2016;51(7):421–429.
- [5] FDA news release: FDA clears first major imaging device advancement for Computed Tomography in nearly a decade. 2021 Sep 30.
- [6] Pourmorteza, A., Symons, R., et al. Photon-counting CT of the brain: in vivo human results and image-quality assessment, *AJNR Am J Neuroradiol*. 2017 Dec; 38(12):2257-2263.
- [7] Rajendran, K., Petersilka, M., Henning, A., et al. First clinical photon-counting detector CT System: technical evaluation. *Radiology* 2022; 000:1-9.
- [8] Willeminck, M., Persson, M., Pourmorteza, A., Pelc, N., Photon-counting CT: technical principles and clinical prospects. *Radiology* 2018; 00:1-20.
- [9] Leng, S., et al. Photon-counting detector CT: system design and clinical applications of an emerging technology. *RadioGraphics* 2019; Vol.39, No. 3.
- [10] Rajendran, K., Petersilka, M., et al. Full field-of-view, high-resolution, photon counting detector CT: technical assessment and initial patient experience. *Phys. Med. Biol.* 2021 Oct 27;66(2):10.
- [11] Si-Mohamed, S., Boccacini, S., et al. Coronary CT angiography with photon-counting CT: first-in-human results *Radiology* 2022 May;303(2):303-313.
- [12] Shefer, E., Altman, A., Behling, R., et al. State of the art of CT detectors and sources: a literature review. *Curr Radiol Rep* 2013; 1(1):76-91.
- [13] Johnson, T., Fink, C., et al. Dual energy CT in clinical practice. Heidelberg, Germany: Springer, 2011.
- [14] McCollough, CH., Leng, S., Yu, L., Fletcher, JG. Dual- and multi-energy CT: principles, technical approaches, and clinical applications. *Radiology* 2015;276(3):637-653.

- [15] Roessl, E. and Proksa, R., “K-edge imaging in x-ray computed tomography using multi-bin photon counting detectors,” *Physics in Medicine and Biology* 52(15), 4679–4696 (2007).
- [16] Si-Mohamed, S., Cormode, D. P., et al. Evaluation of spectral photon counting computed tomography K-edge imaging for determination of gold nanoparticle biodistribution in vivo. *Nanoscale*, 2017, 9, 18246-18257.
- [17] Ostadhossein, F., et al. Multi-“color” delineation of bone micro damages using ligand-directed sub-5 nm hafnia nanodots and photon counting CT imaging. *Advanced Functional Materials*, 2020, 30, 1904936.
- [18] Muenzel, D., et al. Spectral photon-counting CT: initial experience with dual-contrast agent K-edge colonography. *Radiology* 2017, 283, 723-728.
- [19] Blevis, I. X-ray detector for spectral photon counting CT. *Spectral, photon counting computed tomography technology and applications*, CRC Press
- [20] Taguchi, K., Zhang, M., Frey, E., Wang, X., Modeling the performance of a photon counting x-ray detector for CT: energy response and pulse pileup effects. *Med. Phys.* 38 (2), Feb. 2011.
- [21] Alvarez, R. E., Macovski, A., Energy-selective reconstructions in x-ray computerized tomography. *Phys. Med. Biol.* 1976 21 733-44.
- [22] Roessl, E., Proksa, R., K-edge imaging in x-ray computed tomography using multi-bin photon counting detectors. *Phys. Med. Biol.* 52 (2007) 4679-4696.
- [23] Leng, S., Zhou, W., Yu, Z., et al. Spectral performance of a whole-body research photon counting detector CT: quantitative accuracy in derived image sets. *Phys Med Biol* 2017;62(17):7216–7232.
- [24] Liu, X., Persson, M., et al. Spectral response model for a multibin photon-counting spectral computed tomography detector and its applications, *Journal of Medical Imaging* 2(3), 033502 (2015).
- [25] Schmidt, T. G., Barber, R. F., and Sidky, E. Y., A spectral CT method to directly estimate basis material maps from experimental photon-counting data, *IEEE Transactions on Medical Imaging* 36, 1808-1819 (2017).
- [26] Dickmann, J., Maier, J., et al. A count rate-dependent method for spectral distortion correction in photon counting CT. *Proc. Of SPIE Vol. 10573* 1057311-1 (2018).
- [27] Faby, S., Kuchenbecker, S., et al. Performance of today’s dual energy CT and future multi energy CT in virtual non-contrast imaging and in iodine quantification: A simulation study. *Med. Phys.* 2015 Jul;42(7):4349-66.
- [28] Alvarez, R., Estimator for photon counting energy selective X-ray imaging with multibin pulse height analysis, *Med. Phys.* 38(5), May 2011.
- [29] Zhan, X., Wu, S., Hein, I., Markov, N., et al. A study of cross-talk effect in pixelated photon counting detectors and impact to system imaging performance. To be published in *Proc. Of SPIE* 2023.